

Motion Compensated Fan-Beam CT by Enforcing Fourier Properties of the Sinogram

Martin Berger, Andreas Maier, Yan Xia, Joachim Hornegger and Rebecca Fahrig

Abstract—In computed tomography involuntary patient motion can lead to a severe degradation of image quality. Most of the motion estimation methods rely on additional information, such as fiducial markers or an ECG signal. In contrast, data driven motion estimation exists which aims to estimate the motion directly from the acquired projections. This is typically achieved by the optimization of an error metric that is either defined in the image or in the projection domain. In this work, we present a novel data driven error function for motion compensation in fan-beam CT and its combination with a simple motion compensation scheme. The new method operates entirely in the fourier domain of the sinogram, by enforcing zero energy regions of the spectrum. Qualitative and quantitative results show that the proposed method is able to remove most of the motion artifacts, yielding a relative root mean square error of 7.09% compared to 20.35% for the motion corrupted reconstruction.

Keywords—*Computed Tomography, C-arm CT, Motion Compensation, Image Reconstruction*

I. INTRODUCTION

In computed tomography (CT) patient or scanner motion can lead to severe motion artifacts, typically observable as streaking. This is due to the fact that the acquired projections are no longer consistent with the trajectory assumed for image reconstruction. Detection and compensation of such motion during the image reconstruction process can substantially increase the image quality. However, often additional information is necessary to detect the motion. For example external markers which are clearly visible in the projection images can be attached to estimate the patient motion [1]. The assumption here is that the detected surface motion correlates to the motion at the volume of interest (VOI), which might not always be true. In the field of cardiovascular imaging, motion artifacts can be reduced by ECG-gating. Here only a subset of the acquired projections from similar heart phases is built by exploiting information of the ECG signal that was acquired during the scan. However, the ECG data might not correspond exactly with the heart motion and reconstruction of such a subset can also cause undersampling artifacts [2].

To allow for a motion compensated reconstruction independent of additional information sources the motion needs to be directly estimated from the acquired data. This type of motion estimation typically requires an iterative minimization of error metrics, where the motion is estimated such that the error metric is minimized. The metrics can be defined directly in the reconstructed image domain, but also in the sinogram

space [3]. For parallel-beam geometry, it has been shown that the two-dimensional Fourier transform of the sinogram contains triangular shaped regions that have an absolute value close to zero [4]. Recently this concept has been extended to the fan-beam case [5]. In this work we utilize the findings of [5] and propose an error metric and motion estimation scheme that is entirely based in the fourier domain of the sinogram.

II. MATERIALS AND METHODS

A. Fourier Properties of the Sinogram

In Fig. 3(f) an example spectrum of a sinogram is shown which clearly depicts the triangular regions. The size and orientation of these regions depend on the maximum distance of the object to the center of rotation r_p , as well as the source-to-patient distance L and the detector-to-patient distance D . According to [5] the spectral zero regions for a flat detector can be described by

$$\left| \frac{\omega}{\omega - \xi(L + D)} \right| > \frac{r_p}{L}, \quad (1)$$

where ω and ξ are the frequency variables corresponding to the projection angles and the detector rows, respectively. The triangular regions are by definition designed for objects centered in the rotation center. However, potential patient or scanner motion violates this requirement. Hence, the overall energy in the triangular spectral regions increases.

B. Error Measure for Motion Compensation

We now introduce the cumulative energy, i.e. the sum of squared absolute values inside the triangular regions, as an objective function for patient motion correction. The error measure can be written as

$$e(\mathbf{P}) = \left\| \mathbf{F}_\xi \mathbf{P} \mathbf{F}_\omega \circ \mathbf{W} \right\|_{\text{F}}^2, \quad (2)$$

where $\mathbf{P} \in \mathbb{R}^{M \times N}$ is the sinogram with N projections of length M on its columns. $\mathbf{F}_\xi \in \mathbb{R}^{M \times M}$ and $\mathbf{F}_\omega \in \mathbb{R}^{N \times N}$ denote discrete fourier transform (DFT) matrices, corresponding to DFTs along the detector and the projection angles, respectively. $\mathbf{W} \in \mathbb{R}^{M \times N}$ is a binary matrix that evaluates to one where (1) is true and to zero otherwise. Further, $\|\cdot\|_{\text{F}}^2$ is the squared Frobenius norm and \circ denotes the element-wise matrix multiplication.

For the correction of the two-dimensional patient motion we assume simple one-dimensional detector translations. Optimization of (2) requires frequent evaluations of the error function including the 2D fourier transform. We utilize the shift-theorem to move the detector translation after the 1D

Rebecca Fahrig is with the Department of Radiology, Stanford University, Stanford, CA, USA. Martin Berger, Andreas Maier, Yan Xia and Joachim Hornegger are with the Pattern Recognition Lab, Department of Computer Science, Friedrich-Alexander-Universität Erlangen-Nürnberg. This work has been supported by the Research Training Group 1774 "Heterogeneous Image Systems", funded by the German Research Foundation (DFG).

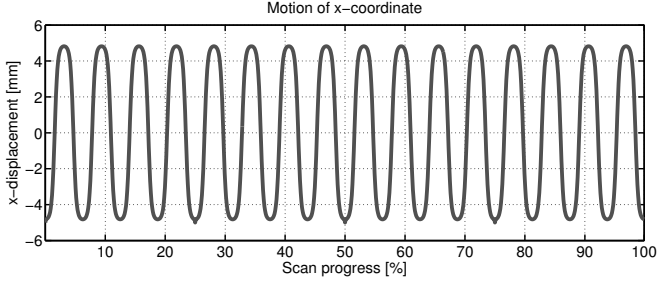


Fig. 1. Simulated periodic translation along the x-axis over the scan progress.

fourier transform along the detector. Let t_n be the translation of the n -th projection, then (2) can be rewritten as

$$[t_1, \dots, t_N] = \arg \min_{[t_1, \dots, t_N]} \left\| ((F_\xi P) T) F_\omega \circ W \right\|_F^2, \quad (3)$$

$$\text{with } T = \begin{pmatrix} e^{-i\frac{2\pi\xi}{M}t_1} & \dots & 0 \\ \vdots & \ddots & \vdots \\ 0 & \dots & e^{-i\frac{2\pi\xi}{M}t_N} \end{pmatrix}.$$

$T \in \mathbb{R}^{N \times N}$ is a matrix that has the phase factors on its diagonal and is zero elsewhere. Note, that $F_\xi P$ is independent of t_n and can thus be precomputed prior to optimization. Thus, additional evaluations of (3) only require a 1D fourier transform along the projection angles.

C. Gradient Computation

For a more robust numerical optimization it is advantageous to have an analytically derived gradient of the cost function [6]. In the following we derive the partial derivatives of (3) with respect to the detector shifts t_n . First, we build the derivative of the Frobenius norm, where $\text{Tr}(\cdot)$ denotes the trace and H the Hermitian operator. We used the identity $\|X\|_F^2 = \text{Tr}(XX^H)$ and define $X = ((F_\xi P) T) F_\omega \circ W$.

$$\frac{\partial}{\partial t_n} \|X\|_F^2 = \text{Tr} \left(\left(\frac{\partial}{\partial t_n} X \right) X^H + X \left(\frac{\partial}{\partial t_n} X \right)^H \right) \quad (4)$$

To evaluate (4) we need to derive the partial derivatives of X .

$$\begin{aligned} \frac{\partial}{\partial t_n} X &= \frac{\partial}{\partial t_n} \left(((F_\xi P) T) F_\omega \circ W \right) \\ &= \left((F_\xi P) \frac{\partial}{\partial t_n} T \right) F_\omega \circ W \\ &= \left((F_\xi P) \left(-i\frac{2\pi\xi}{M} \exp(-i\frac{2\pi\xi}{M}t_n) J^{nn} \right) \right) F_\omega \circ W \\ &= (E) F_\omega \circ W \end{aligned} \quad (5)$$

Here J^{nn} is a single-entry matrix, which is one at (n, n) and zero elsewhere. $E \in \mathbb{R}^{M \times N}$ can be interpreted as follows. First we shift the projections by t_n directly in the fourier domain. Subsequent multiplication by $-i\frac{2\pi\xi}{M}$ is equivalent to the derivative over the shifted projections. With J^{nn} we then select the n -th projection and set the others to 0. Because E has only one non-zero column, the fourier transform over the rows, F_ω , degenerates to a simple vector multiplication

$$(E) F_\omega = e_n f_n^\omega,$$

Parameter	Symbol/Unit	High-quality	Low-quality
Source-patient-distance	L	600	600
Detector-patient-distance	D	0	0
Approx. object extent [mm]	r_p	122.5	122.5
#Detector cells	M	1240	620
Detector spacing [mm]	du	0.25	0.5
#Projections	N	892	240
Angular spacing [degree]	$d\beta$	0.404	1.5
Reconstruction size	$R_x \times R_y$	2048 × 2048	2048 × 2048
Pixel size	[mm × mm]	0.125 × 0.125	0.125 × 0.125
Absorption model	-	monochromatic	monochromatic
Photon Energy	[keV]	80	50
#Photons	-	-	30000

TABLE I. SIMULATION PARAMETERS USED FOR THE EVALUATION.

where $e_n \in \mathbb{R}^{M \times 1}$ is the n -th column of E and $f_n^\omega \in \mathbb{R}^{1 \times N}$ is the n -th row of F_ω . Considering the use of a fast fourier transform (FFT) the complexity reduces from $\mathcal{O}(MN \log(N))$ to $\mathcal{O}(MN)$.

Because X is already computed when evaluating the error function (3), the gradient computation does not require an additional FFT and can be implemented efficiently.

III. EVALUATION AND RESULTS

A. Evaluation

To evaluate our method we used the central slice of the FORBILD head phantom¹. The experiments consisted of a high quality, noise free scan, but also a low quality, noisy simulation to investigate the method's behaviour under more realistic conditions. The geometric, as well as the reconstruction parameters used for the simulations are presented in Table I.

Affine motion of the head phantom has been simulated as an accelerated periodic translation around the x-axis, denoted as $t_x(\beta)$. The motion model can be described by

$$t_x(\beta) = \hat{t}_x \left(\frac{2}{1 + \exp(a \cos(k\beta))} - 1 \right), \quad (6)$$

where \hat{t}_x is the amplitude, k is the number of periods per scan, and a is an acceleration factor. For our simulation we chose $\hat{t}_x = 5$ mm, $k = 16 \text{ deg}^{-1}$ and $a = 4$. Fig. 1 depicts a plot of the x-axis translation over the scan progress.

The evaluation procedure for both, low-quality and high-quality simulations, was as follows. First we analytically computed the sinogram for the motion corrupted but also for the motion free case. As a reference we also rendered the phantom directly in the reconstruction space, where we used the attenuation coefficients as pixel intensities. Note that the attenuation coefficients are energy dependent, hence the low-quality differs from the high-quality ground truth phantom. All simulations have been carried out using the open source software CONRAD [7].

For the minimization of the cost-function (3) we used the L-BFGS algorithm, where we provided the partial derivatives as given by (4). To compute the mask W the object extent r_p is required. We estimated r_p from the sinogram by measuring

¹www.imp.uni-erlangen.de/phantoms

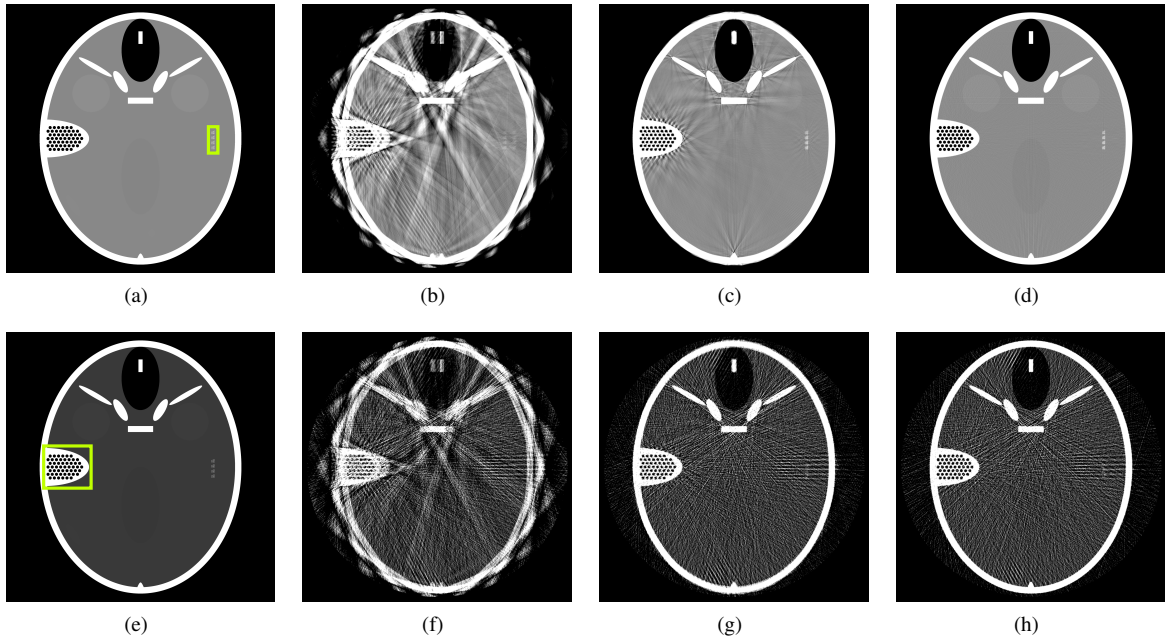


Fig. 2. Qualitative reconstruction results for the high-quality (top row) and the low-quality (bottom row) simulations. From left to right: Ground truth rendering, motion corrupted, motion corrected and the motion free reconstruction. Visualization windows are $[0.07, 0.27]$ for the top and $[0.07, 0.80]$ for the bottom row.

the maximum distance between the projection boundaries (see Table I). The optimization was done repeatedly using a multi-resolution approach. The sinogram scaling factors were 0.25, 0.5 and 1 and a zero vector was used for initialization. The optimized shifts were incorporated into the reconstruction as described in [8].

For a quantitative evaluation we computed the relative root mean square error (rRMSE) of the motion corrupted, the corrected and the motion-free reconstruction with respect to the corresponding ground truth. The rRMSE is defined as

$$rRMSE(\mathbf{R}, \mathbf{G}) = \frac{1}{\hat{I}_g} \|\mathbf{R} - \mathbf{G}\|_F$$

where \mathbf{R} is the reconstructed and \mathbf{G} the ground truth image and \hat{I}_g the intensity range of \mathbf{G} .

B. Results

Figure 2 shows the reconstruction results for the high (top row) and low-quality (bottom row) simulations. In both cases the image quality improved substantially when comparing the corrected to the motion corrupted reconstructions. The proposed method was able to restore edges, especially at the lateral boundaries. However, in the high-quality simulations we still observe some residual streaking artifacts compared to the reference reconstruction where no motion was present. For the low-quality simulations our approach yielded comparable results to the motion free reconstruction.

The sinograms and their spectra are depicted in Fig. 3 for the high-quality simulations. The motion and its correction is clearly visible in the spatial domain. This observation is supported by the corresponding spectra, where we clearly see a reduced energy in the superimposed triangular regions. This is in agreement with the actual error function values provided in Table II.

Measure		With motion	Corrected	Reference
High-quality	rRMSE [%]	20.35	7.09	2.48
	$e(\mathbf{P}) [\times 10^6]$	1648.49	32.35	0.34
Low-quality	rRMSE [%]	25.12	13.97	12.57
	$e(\mathbf{P}) [\times 10^6]$	109.55	6.32	4.12

TABLE II. ERROR FUNCTION AND RMSE VALUES FOR THE MOTION CORRUPTED, THE CORRECTED AND THE REFERENCE SPECTRA.

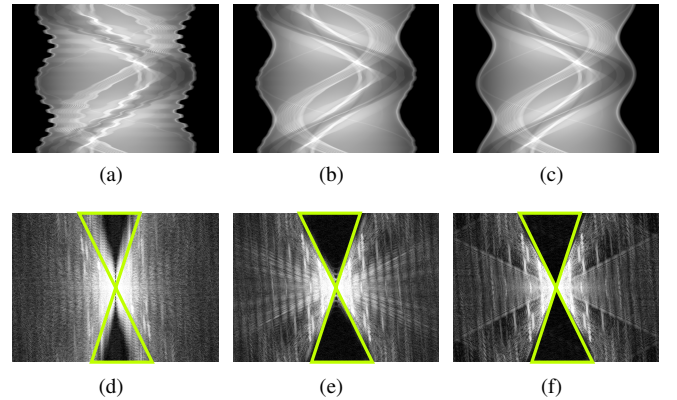


Fig. 3. Sinograms (top row) and their logarithmically scaled spectra (bottom row) for the noise-free projections. From left to right: motion corrupted, motion corrected and the motion free reference. Visualization windows are $[1.0, 5.5]$ for the sinograms and $[1.5, 5.0]$ for the log-spectra.

In Fig. 4 we can see a detailed view of the reconstructed area around the phantom's resolution pattern for the noise-free data. In comparison to the motion corrupted reconstruction, where the pattern is no longer visible, the proposed method could restore the pattern adequately. However, we can see some loss of information compared to the motion free reconstruction. For the noisy data a close-up of the phantom's ear is shown in Fig. 5. Compared to the non-corrected reconstruction, our

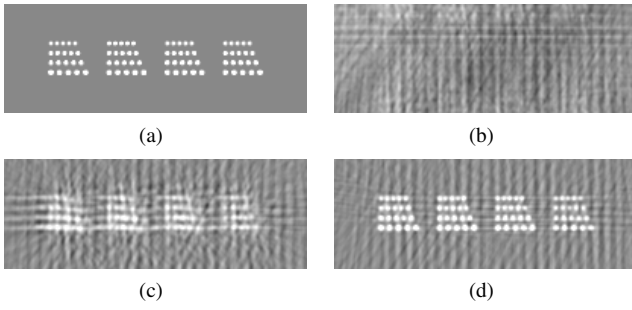


Fig. 4. The reconstructed resolution pattern for the high quality simulations. From (a) to (d): Ground truth, motion corrupted, motion corrected and motion free reconstruction. The region's position is superimposed in Fig. 2(a).

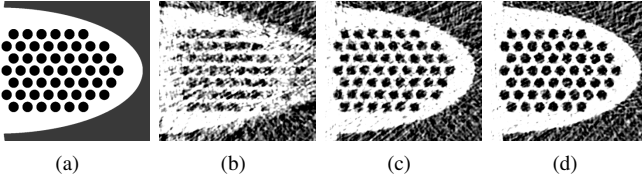


Fig. 5. The reconstructed left ear in case of the noisy data. From left to right: Ground truth, motion corrupted, motion corrected and motion free reconstruction. The region's position is superimposed in Fig. 2(e).

method was able to restore the encapsulated air bubbles, yielding similar results to those seen in the motion free reconstruction.

To get an impression of how accurate the translations were estimated, we forward projected the moving phantom's center position to the detector for each projection. In Fig. 6 the forward projected (gray, solid line) and the estimated translations (orange, dashed line) are plotted for the high-quality simulations. The plot shows that our approach reliably estimated the translational effect of the motion. A very similar result was obtained for the low-quality case.

IV. DISCUSSION

Our evaluation shows promising results for ideal high-quality data without noise. Because the error function is defined in the Fourier domain we show that the method also works for low-quality simulations which contain a significant amount of noise. Compared to the reconstructions without motion correction, our approach improved image quality substantially. For the low-quality case the motion compensated reconstruction yielded comparable results to those of the reference reconstruction without motion. This is in line with the achieved quantitative results as shown in Table II.

In case of the high-quality data our method was able to restore most of the structures, yet we still observe some remaining motion-based artifacts. This limitation might be due to our relatively simple motion model which only takes detector shifts into account. Shifting the detector can effectively only compensate for that part of the motion that was parallel to the detector. It does not take potential scaling of the projections into account that occur from motion orthogonal to the detector. The resulting residual artifact is represented by small ripples in the corrected sinogram in Fig. 3(b). In Fig. 6 we show that when we only consider the motion parallel to the detector, the

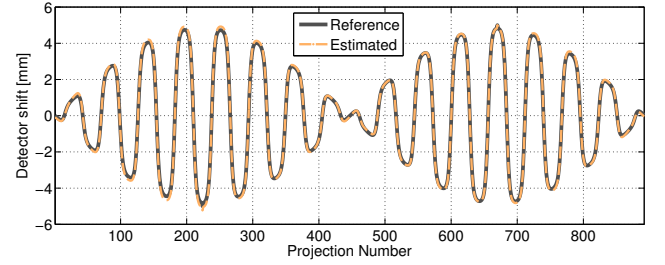


Fig. 6. Forward projection of the phantom's center (solid line) compared to the estimated detector shifts (dashed line), for the high-quality data.

optimization of our error measure is capable of estimating the motion with high accuracy.

A simulated periodic motion along the x-axis was used for this proof of concept. Evaluations with a more realistic patient motion will be part of future work. Further, we plan to extend the underlying Fourier properties to a cone-beam formulation where we also want to incorporate short-scans. This would then allow its application on real C-arm CT data.

V. CONCLUSION

In this work we present a novel data driven error function for motion compensation in fan-beam CT. Further we introduce its combination with a simple motion compensation scheme by incorporating projection shifts. We also derive the gradient and show that its computation can be implemented efficiently. Our qualitative and quantitative results show that the proposed method is able to correct most of the motion artifacts.

REFERENCES

- [1] J.-H. Choi, R. Fahrig, A. Keil, T. F. Besier, S. Pal, E. J. McWalter, G. S. Beaupré, and A. Maier, "Fiducial marker-based correction for involuntary motion in weight-bearing C-arm CT scanning of knees. Part I. Numerical model-based optimization," *Medical Physics*, vol. 40, no. 9, p. 091905, 2013.
- [2] C. Schwemmer, C. Rohkohl, G. Lauritsch, K. Müller, and J. Hornegger, "Residual motion compensation in ECG-gated interventional cardiac vasculature reconstruction," *Physics in Medicine and Biology*, vol. 58, no. 11, p. 3717, 2013.
- [3] S. Ens, J. Ulrici, E. Hell, and T. Buzug, "Automatic motion correction in cone-beam computed tomography," in *Nuclear Science Symposium Conference Record (NSS/MIC)*, 2010 IEEE, 2010, pp. 3248–3251.
- [4] P. R. Edholm, R. M. Lewitt, and B. Lindholm, "Novel Properties Of The Fourier Decomposition Of The Sinogram," in *Proc. SPIE 0671, Physics and Engineering of Computerized Multidimensional Imaging and Processing*, T. F. Budinger, Z.-H. Cho, and O. Nalcioglu, Eds. International Society for Optics and Photonics, 1986, pp. 8–18.
- [5] S. R. Mazin and N. J. Pelc, "Fourier properties of the fan-beam sinogram," *Medical Physics*, vol. 37, no. 4, pp. 1674–80, 2010.
- [6] J. Nocedal and S. J. Wright, *Numerical Optimization*. Springer New York, 1999, vol. 2.
- [7] A. Maier, H. G. Hofmann, M. Berger, P. Fischer, C. Schwemmer, H. Wu, K. Müller, J. Hornegger, J.-H. Choi, C. Riess *et al.*, "CONRAD A software framework for cone-beam imaging in radiology," *Medical Physics*, vol. 40, no. 11, p. 111914, 2013.
- [8] D. Schaefer, J. Borgert, V. Rasche, and M. Grass, "Motion-Compensated and Gated Cone Beam Filtered Back-Projection for 3-D Rotational X-Ray Angiography," *Medical Imaging, IEEE Transactions on*, vol. 25, no. 7, pp. 898–906, 2006.